ACS NANO
Cite This: ACS Nano 2017, 11, 12562–12572
www.acsnano.org

ARTICLE

Dissolution of Monocrystalline Silicon Nanomembranes and Their Use as Encapsulation Layers and Electrical Interfaces in Water-Soluble Electronics

Yoon Kyeung Lee,[†,‡,§,?] Ki Jun Yu,[¶,?] Enming Song,[‡,§,#] Amir Barati Farimani,[$] Flavia Vitale,[□,■,○,●] Zhaoqian Xie,[▽,▼,⬡,∞] Younghee Yoon,[‡,§] Yerim Kim,[‡,§] Andrew Richardson,[○,●,△] Haiwen Luan,[▽,▼,⬡] Yixin Wu,[⬡,∫] Xu Xie,[‡] Timothy H. Lucas,[○,●,△] Kaitlyn Crawford,[ϕ] Yongfeng Mei,[#] Xue Feng,[∞] Yonggang Huang,[■] Brian Litt,[□,○,●,▲] Narayana R. Aluru,[‖] Lan Yin,[*,∫] and John A. Rogers[*,⬡,δ,λ,▼,×,⬢]

[†]Department of Chemistry, [‡]Department of Materials Science and Engineering, [§]Frederick Seitz Materials Research Laboratory, and [‖]Mechanical Science and Engineering, Beckman Institute for Advanced Science and Technology, University of Illinois at Urbana—Champaign, Urbana, Illinois 61801, United States

[¶]School of Electrical and Electronic Engineering, Yonsei Univerisity, Seoul 03722, Republic of Korea

[#]Department of Materials Science, Fudan University, Shanghai 200433, China

[$]Department of Chemistry, Stanford University, Stanford, California 94305, United States

[□]Department of Neurology, [■]Department of Physical Medicine and Rehabilitation, [○]Center for Neuroengineering and Therapeutics, [●]Perelman School of Medicine, [△]Department of Neurosurgery, [▲]Department of Bioengineering, School of Engineering and Applied Sciences, Penn Center for Health, Devices & Technology, University of Pennsylvania, Philadelphia, Pennsylvania 19104, United States

Departments of [▽]Civil and Environmental Engineering, [▼]Mechanical Engineering, and [⬡]Materials Science and Engineering, [⬢]Center for Bio-Integrated Electronics, Departments of [δ]Biomedical Engineering, [λ]Chemistry, [×]Electrical Engineering and Computer Science, and Neurological Surgery, Simpson Querrey Institute for Nano/biotechnology, McCormick School of Engineering and Feinberg School of Medicine, Northwestern University, Evanston, Illinois 60208, United States

[∞]AML, Department of Engineering Mechanics, Center for Mechanics and Materials, and [∫]School of Materials Science and Engineering, Tsinghua University, Beijing 100084, China

[ϕ]Materials Science and Engineering University of Central Florida, Orlando, Florida 32816, United States

Supporting Information

ABSTRACT: The chemistry that governs the dissolution of device-grade, monocrystalline silicon nanomembranes into benign end products by hydrolysis serves as the foundation for fully eco/biodegradable classes of high-performance electronics. This paper examines these processes in aqueous solutions with chemical compositions relevant to ground-water and biofluids. The results show that the presence of $Si(OH)_4$ and proteins in these solutions can slow the rates of dissolution and that ion-specific effects associated with Ca^{2+} can significantly increase these rates. This information allows for effective use of silicon nanomembranes not only as active layers in eco/biodegradable electronics but also as water barriers capable of providing perfect encapsulation until their disappearance by dissolution. The time scales for this encapsulation can be controlled by introduction of dopants into the Si and by addition of oxide layers on the exposed surfaces.

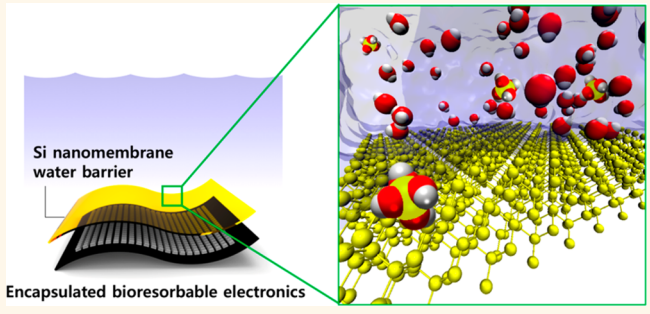

continued...

Received: September 20, 2017
Accepted: November 27, 2017
Published: November 27, 2017

DOI: 10.1021/acsnano.7b06697
ACS Nano 2017, 11, 12562–12572

The former possibility also allows the doped silicon to serve as an electrical interface for measuring biopotentials, as demonstrated in fully bioresorbable platforms for *in vivo* neural recordings. This collection of findings is important for further engineering development of water-soluble classes of silicon electronics.

KEYWORDS: *bioresorbable electronics, transient electronics, silicon dissolution, encapsulation, water barrier*

One of the most attractive features of modern electronic devices is their ability to operate in an almost perfectly reliable fashion, with little to no degradation over exceptionally long periods of operation. Transient electronics is a class of technology designed to offer the opposite behavior, in which the constituent materials disappear, disintegrate, or otherwise change in some controlled physical or chemical way after a period of stable function.[1] A subset of transient technology involves biologically and environmentally resorbable devices that dissolve in biofluids or groundwater into benign end products.[1−5] Although certain classes of passive biomedical devices such as resorbable sutures and polymer matrices for drug release adopt such transient characteristics, it is only through recent research that similar modes of operation are now possible with active electronic systems, including those that use high-performance semiconductors, conductors, and dielectrics.[6−8] Envisioned applications include bioresorbable diagnostic/therapeutic devices that avoid long-term adverse effects and secondary surgical procedures and eco-resorbable consumer gadgets that minimize the costs and health risks associated with waste disposal and recycling.

Of the various biodegradable electronic materials that now exist as options in transient electronics, device-grade, monocrystalline silicon is notable because of its potential to support high-performance devices that align, at least partly, with conventional, nontransient technologies. Recent studies of dissolution of monocrystalline silicon nanomembranes (Si NMs) in aqueous environments provide critical information on rates of hydrolysis in physiological and environmental conditions. Experimental and theoretical efforts offer insights into important characteristics and mechanisms of this chemistry. Specifically, the data suggest that silicon undergoes hydrolysis with catalyzing effects of ions present in the surrounding water, to generate silicic acid ($Si(OH)_4$) and hydrogen as final products.[1,3,6,9] Direct measurements of H_2 evolution and the Si dissolution rates support the stoichiometry of the proposed reaction ($Si + 4H_2O \rightarrow Si(OH)_4 + 2H_2$).[11,29] The process proceeds without reactive diffusion of water into the silicon or of water permeation through defect sites, as indicated by the linear dependence of the thicknesses of Si NMs on reaction time. Rates of 1−100 nm/day occur at near neutral pH in saline solutions, depending on detailed experimental conditions, consistent with historical studies of silicon etching in alkaline and HF-containing etchants, where variations in step/defect densities, distributions of interface energy states, surface oxides, and metallic/organic contamination can affect the observations.[10−15] Additionally, doping with boron and phosphorus dramatically decelerates the dissolution at concentrations above 10^{19} cm^{-3}, consistent with etching behavior in high-pH solutions.[9] Here, we extend these collective studies to examine effects of proteins and divalent cations (Ca^{2+} and Mg^{2+}) and the role of silicic acid ($Si(OH)_4$) as a product of dissolution and a ubiquitous component of natural and biological fluids, commonly at concentrations between 10^0 and 10^1 ppm.

The slow rates of dissolution and the perfect monocrystalline nature of the Si NMs also enable their use as bioresorbable water barriers to encapsulate implantable electronic systems. Compared to alternatives based on spin-cast polymers and inorganic materials (oxides, nitrides, *etc.*) formed by physical or chemical vapor deposition,[1,16,17] Si NMs ensure zero water transmission but retain bioresorbable forms, where submicron thicknesses are sufficient for device lifetimes in the range of several days to years. Additional results presented here demonstrate these capabilities, along with two strategies for extending the lifetime: decelerating the dissolution rate by use of doping at high concentrations and delaying the initiation of dissolution by use of thin layers of SiO_2 grown on the silicon surface. Reactive molecular dynamics simulations provide insights into the reactions that occur at the Si/water and SiO_2/water interfaces. Experiments show the ability to form flexible electrode arrays using thin patterned Si NMs on Mo, in fully bioresorbable formats for *in vivo* neural recordings.

RESULTS AND DISCUSSION

Figure 1 summarizes the rates of dissolution of Si NMs in phosphate buffered saline (PBS, 1×) with different concentrations of protein, $Si(OH)_4$, and cations. Figure 1a describes reductions in thickness of Si NMs (p-Si, boron, 8.5−11.5 Ω·cm (10^{15} cm^{-3}), (100), SOITEC) by hydrolysis in PBS solutions with different albumin concentrations at 37 °C. The experiments involve 0.25 mm^2 pieces of silicon-on-insulator (SOI) wafers that have a top silicon layer (*i.e.*, the Si NM) with 200 nm thickness immersed in 30 mL of solution immediately after exposure to UV ozone and buffered oxide etchant, to form a hydrogen-terminated surface. Addition of bovine serum albumin into PBS provides access to a wide range of protein concentrations relevant to those in natural and biological fluids; the latter have concentrations between 10^{-2} and 10^2 g/L (~80 g/L in blood, ~20 g/L in interstitial fluids, 0.1−1 g/L in saliva and aqueous humor, 0.01−0.1 g/L in urine).[18,19] Analysis of spectroscopic reflectance data collected from the SOI wafer determines the thickness of the Si NM (Figure S1a). Figure 1b compares rates of dissolution of Si as a function of albumin concentration in PBS. The values fall between 59 ± 0.5 (error defined as error in slope in linear fitting of thickness average at times) and 35 ± 0.4 nm/day. The deceleration likely follows from adsorption of protein on the silicon surface (0.5 to 1.5 nm, slightly varying with a kind of protein) and its resulting effects on limiting diffusive access of water to the surface.[20−22] Although the current studies focus on albumin, which is the most abundant protein in blood plasma, protein-specific effects on the deceleration of Si dissolution may exist due to the differences in their interaction to the Si surface.

Figure 1c compares the rates of dissolution as a function of $[Si(OH)_4]$ in PBS with three different albumin concentrations at 37 °C. Here, the $Si(OH)_4$ results from a Si standard solution (Si 1000 ppm, Sigma-Aldrich) prepared by dissolving high-purity silicon metal in 2% NaOH solution. After dilution to 100 ppm of Si, adjusting the pH and salt composition returns these values to those of the original PBS solution. In contrast to extensive data on the role of $Si(OH)_4$ in dissolution and condensation of silica,[23−26] its influence on the dissolution of Si has not been examined previously. The data in Figure 1c show reductions in the rates with increasing $[Si(OH)_4]$ at all protein concentrations,

DOI: 10.1021/acsnano.7b06697
ACS Nano 2017, 11, 12562−12572

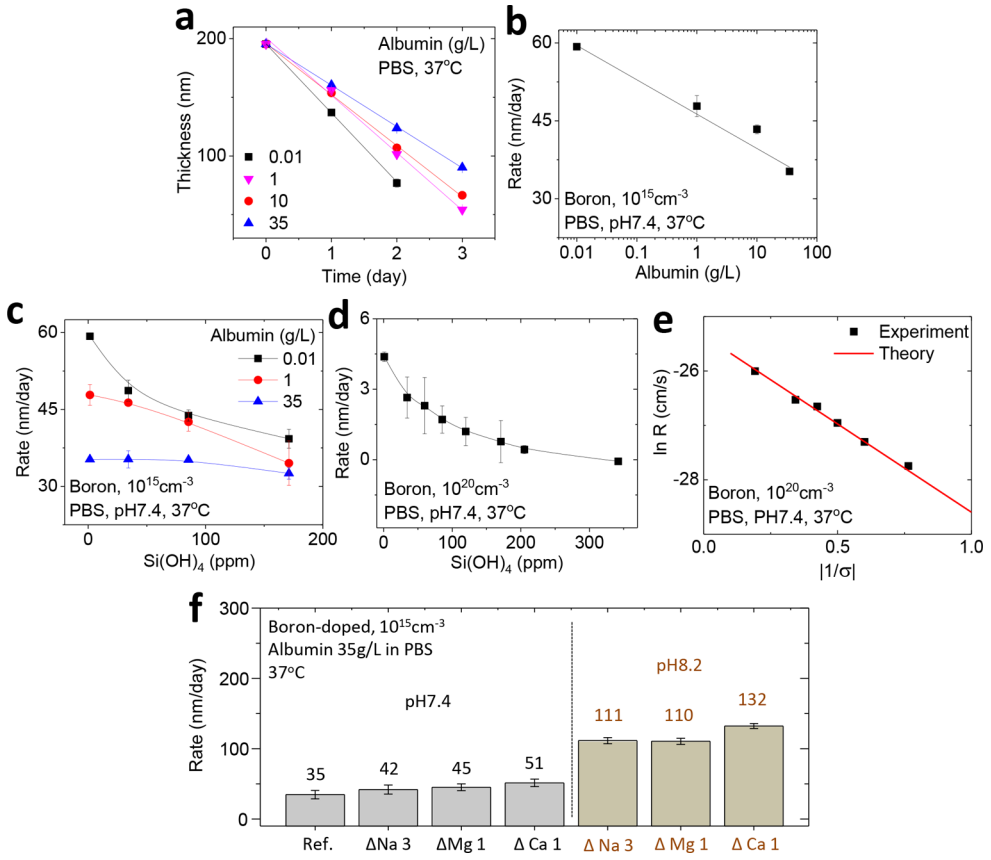

Figure 1. Dependence of the rate of dissolution of Si on the presence of protein, silicic acid, Ca^{2+} and Mg^{2+} in phosphate buffered saline (PBS, pH 7.4). (a) Change in thickness of p-Si NMs (boron, 10^{15} cm^{-3}) as a function of time during dissolution. (b) Dependence of the dissolution of p-Si on the presence of protein. (c) Dependence of the dissolution of p-Si on the presence of $Si(OH)_4$ with different protein concentrations. (d) Dependence of the dissolution of p^+-Si (boron, 10^{20} cm^{-3}) on the presence of $Si(OH)_4$. (e) Polynuclear dissolution model for p^+-Si dissolution. (f) Cation-specific effects on the rate of dissolution of p-Si.

qualitatively consistent with mechanistic reasoning based on the chemistry of Si hydrolysis ($Si + 4H_2O \rightleftharpoons Si(OH)_4 + 2H_2$). Also, an increased dependence of the rate on $[Si(OH)_4]$ follows reduced protein concentration, that is, for (0.01g/L), 59 ± 0.5 to 39 ± 1.9 nm/day; for (35g/L), 39 ± 0.4 to 33 ± 1.1 nm/day. Notably, the rate is non-negligible even in solutions at the saturation level of $Si(OH)_4$ (~185 ppm of $Si(OH)_4$ at 37 °C),[27] where this species starts to polymerize to SiO_2, due to rates of Si hydrolysis that are faster than those associated with conversion of $Si(OH)_4$ to Si or SiO_2 with 10^0–10^2 ppm of $Si(OH)_4$ concentrations. By comparison, the rates of dissolution of SiO_2 have enhanced dependence on $[Si(OH)_4]$, with values that approach zero at the same $Si(OH)_4$ saturation level.[23−26] (Experiments in protein-free, purified PBS solutions show large variations and spatial nonuniformities in the dissolution rates depending on detailed conditions, likely due to uncontrolled levels of organic contaminants in ambient conditions.[13,28] The addition of small amounts of organic molecules such as proteins or phenol red as a pH indicator yields reproducible rates across individual samples and between experiments.)

Figure 1d summarizes the dependence of the rate of dissolution of highly doped Si (p^+-Si, boron, 10^{20} cm^{-3}) on $Si(OH)_4$ as an additional point of comparison. The rates decrease rapidly with increasing $[Si(OH)_4]$ and virtually cease at ~200 ppm of $Si(OH)_4$, similar to the behavior of SiO_2. The slow rates of dissolution and the strong dependence on $Si(OH)_4$ for this case can be explained by the presence of a surface layer of SiO_2, as supported by previous ellipsometric measurements that show a stable oxide on highly doped Si (~1 nm) and barrier-less oxidation pathways in the presence of both boron and phosphorus impurities.[30−33] Lightly doped Si, by comparison, has a porous passivation layer that is permeable to water molecules and that continuously grows in parallel with Si dissolution.[32] Figure 1e presents fits of experiment data to a polynuclear dissolution model previously used to describe the dissolution of amorphous SiO_2 in the presence of $Si(OH)_4$.[26] This model explains the dependence of SiO_2 dissolution on $[Si(OH)_4]$ by reduced step propagation rates and increased activation energy for the formation of vacancy (or highly reactive) sites where dissolution starts to spread. According to the model, the rate can be expressed as

$$\ln R = \ln(hs{\cdot}A) - \frac{\pi\alpha^2\omega h}{(kT)^2}\cdot\frac{1}{|\sigma|}$$

where R is the volume of dissolution nuclei formed per unit area of surface and time, h is the height of the vacancy, S is the surface area affected by each nucleation event, A is a pre-exponential factor for nucleation rate, ω is the specific volume of the molecule, α is the local interfacial free energy, k is Boltzmann constant, and T is the temperature.[26] The degree of undersaturation is $\sigma = \ln(C/Ce)$, where C and Ce (185 ppm) are experimental and equilibrium concentrations of $Si(OH)_4$, respectively. The equation indicates that the logarithm of the rate of removing a unit of material from the surface has a squared dependence on the interfacial free energy (α) to create a new surface with highly reactive

DOI: 10.1021/acsnano.7b06697
ACS Nano 2017, 11, 12562−12572

Si atoms exposed. Considering the presence of a surface oxide layer on silicon and dissolution of this oxide,[32] we used parameters of $\omega_{SiO_2} = 4.54 \times 10^{-23}$ cm^3/molecule, height $h_{SiO_2} = 2.17$ Å, and $T = 310.15$ K in simulations for the dissolution of amorphous SiO_2.[26] Fitting experimental data for highly doped Si, as shown in Figure 1e, to this model yields an interfacial free energy $\alpha = 40$ mJ/m^2, slightly lower than that of amorphous colloidal/biogenic silica and approximately a factor of 2 smaller than that for high-density SiO_2 such as quartz or thermally grown oxide.[26] By comparison, using parameters of Si crystal structures ($\omega_{Si} = 1.99 \times 10^{-23}$cm^3/molecule, $h_{Si} = 1.36$ Å) in the fit yields an unlikely large value of 84 mJ/m^2.

Accelerated dissolution occurs at high pH and in the presence of divalent cations (Ca^{2+} and Mg^{2+}), as in Figure 1f. Experiments to define the latter effects involve 1 mM of $CaCl_2$ and $MgCl_2$ separately added to protein-containing PBS solutions from their 1 M standard solutions. A concentration of 1 mM is comparable to that found in naturally occurring biofluids. Figure 1f describes the accelerating effect of Ca^{2+} at pH values between 7.6 and 8.2. Solutions containing $CaCl_2$ dissolve Si faster than the solutions with NaCl or $MgCl_2$ at the same ionic strength. Since the $[Cl^-]$ in $CaCl_2$ and $MgCl_2$ solutions is lower than that in a NaCl solution at the same ionic strength, the observed acceleration in $CaCl_2$ solution can be attributed to the cation. The results follow similar trends reported for dissolution of quartz and silica, where Ca^{2+} accelerates the hydrolysis of SiO_2 more effectively than Na^+ at near neutral pH.[25,26] Here, Ca^{2+} may have an increased ability to deprotonate surface silanol groups formed by absorption of water to Si surface and/or to enhance the reactivity of water and siloxane groups as suggested in previous studies of SiO_2 dissolution.[34−37] A discussion of the process of forming silanol and siloxane groups on the Si surface appears subsequently.

Figure 2 summarizes results of Si NM dissolution in various types of saline solutions. Environmental and biological fluids cover a range of pH values and concentrations of ions and organic compounds. For example, the pH of common biological and environmental solutions can be as low as 4.5 as in urine and sweat and as high as 8.4 as in carbonate-containing solutions such as seawater. In terms of salinity, rivers and oceans contain 0.1 g to >50 g/L solid contents mostly associated with dissolved cations (Na^+, Ca^{2+}, and Mg^{2+}) and anions (Cl^-, HCO_3^-, SO_4^{2-}, and silica). In extracellular biofluids, the concentrations are strictly regulated to within 8−20 g/L, mostly composed of NaCl. Biofluids also contain high-energy nutrients such as glucose and proteins for cell metabolism. Figure 2a,b shows changes in color and thickness associated with 100 μm^2 patterns of Si NMs (boron, 10^{15}cm^{-3}) with thicknesses of 200 nm in different saline solutions. Here, artificial perspiration has lower pH and higher NaCl concentration than the other fluids (pH 4.5). Bovine serum contains salt compositions similar to those of PBS, but with additional bicarbonate (15−30 mM) divalent cations (~1 mM Mg^{2+}, Ca^{2+}) and various proteins (56 g/L in total) (see Table S1). Hank's balanced salt solutions (HBSS) at two different pH values (7.6 and 8.2) and in formulations with and without divalent cations (Ca^{2+}, Mg^{2+}) provide additional points of comparison. Figure 2b indicates that the lowest rates occur in perspiration due primarily to its low pH; the highest rates occur in pH 8.2 HBSS with Ca^{2+} and Mg^{2}+, consistent with previous observations of enhanced dissolution by Ca^{2+}. Figure 2c summarizes the rates in various types of environmental and simulated body fluids at room temperature and 37 °C. Water purified by reverse osmosis, free from ions and larger molecules, shows the lowest rates (0.01 nm/day at 25 °C, 0.2 nm/day at 37 °C), while tap water, known to contain 30−40 ppm of Na^+ and Ca^{2+} and organic/inorganic contaminants, leads to higher rates (0.7 ± 0.1 nm/day at 20 °C, 2.6 ± 0.4 nm/day at 37 °C). Artificial sweat shows slower rates of dissolution than tap water (0.5 ± 0.1 nm/day at 37 °C) due to its low pH despite its high NaCl concentration. Serum dissolves Si even at higher rates (3.5 ± 0.5 nm/day at 20 °C, 21 ± 0.4 nm/day at 37 °C) than these water samples

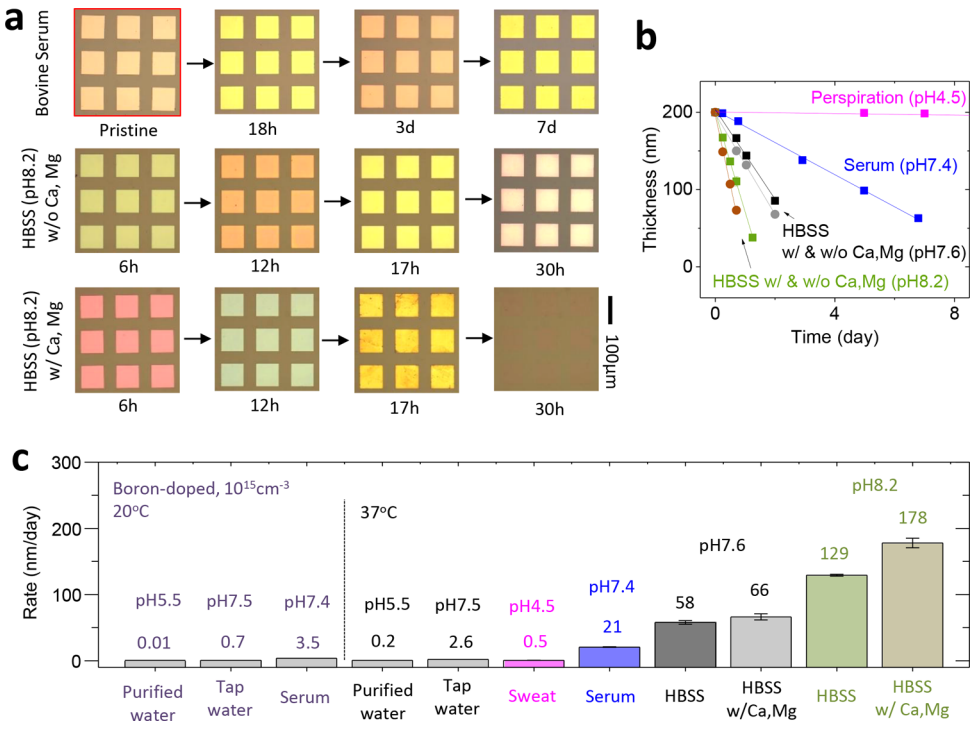

Figure 2. Rate of dissolution of Si NMs in aqueous solutions. (a) Optical images of the surface of the Si. (b) Change in thickness of p-Si NMs in simulated biofluids. (c) Rates of dissolution in different aqueous solutions.

DOI: 10.1021/acsnano.7b06697
ACS Nano 2017, 11, 12562−12572

due to its high salinity but slower rates than those of HBSS due to its protein content.

The observation that hydrolysis of Si NMs proceeds by surface reactions only, in a predictable manner without diffusion through defects or pinholes, creates the possibility for their use as temporary water barriers in bioresorbable electronic systems. Here, the defect-free, monocrystalline nature of the Si NMs leads to zero water transmission even for submicron thicknesses. Knowledge of the rates for dissolution allows design selection to match lifetime requirements for targeted applications. Soak tests using setups that incorporate thin films of magnesium (Figure 3a) underneath Si NMs facilitate evaluation of barrier properties owing to the visible corrosion of the Mg that follows contact with water.[38] Results obtained with spin-cast layers of poly(lactic-*co*-glycolic acid) (PLGA, 5 μm) and electron beam deposited films of SiO_2 (200 nm), instead of Si NMs, indicate almost immediate failure (<10 min) due to soaking in PBS (Figure S2) as a result of water permeation through the materials themselves and through pinhole defects, respectively. Figure 3b shows the rates of dissolution of Si, where a 1.5 μm thick Si membrane survives for ~10 months with a dissolution rate of 4.8 ± 0.2 nm/day at 37 °C. Figure 3c presents an image of an intact Mg pad captured after 2 months of soaking in PBS. Accelerated tests performed at 70 °C (Figure 3d) yield dissolution rates of 67 ± 0.2 nm/day and corrosion of the Mg pad abruptly at 23 ± 4 days.

Figure 4 presents two strategies to modulate the lifetime of this Si NM encapsulation without changing the thickness, the first of which exploits high doping concentrations (Figure 4a, p^+-Si, boron, 10^{20} cm^{-3}). The dissolution of p^+-Si follows the same dependence on salinity, Ca^{2+} concentration, and pH as that of p-Si, but with overall slower rates. Significant deceleration (~40×) in bovine serum compared to that in p-Si suggests that the p^+-Si can enable encapsulation lifetimes of several years even with submicron thicknesses (~180 nm/year). The second strategy involves chemically functionalizing the Si surface to reduce its reactivity. Options in Si−C and Si−O chemistries provide a wide range of barrier lifetimes by delaying initiation of the Si dissolution.[39,40] A simple approach exploits growth of surface oxides at low temperatures by exposure to UV ozone (UVO) or O_2 plasma. The oxide thickness saturates at ~20 nm after 20 min exposure to O_2 plasma and at ~3 nm after 2 h exposure to UVO (Figure S3). Results of studies summarized in Figure 4b demonstrate a delayed initiation of Si dissolution by ~10 and ~30 days, with 3 nm UVO-grown oxide and 20 nm plasma-grown oxide, respectively. Relatively large variations in dissolution rate after initiation may originate from nonuniform thicknesses of the oxides, consistent with the surface morphologies observed by atomic force microscopy (Figure 4c).

Figure 5 presents results of reactive molecular dynamics (RMD) simulations of NMs of Si and SiO_2 (~1.2 nm thickness) designed to reveal atomic scale interactions between Si atoms and water molecules. Here, the Si(100) NM consists of 6 atomic layers of Si with 100 Si surface atoms (atomic density 2.33 g/cm^3, Figure 5a). The SiO_2 NM consists of 283 SiO_2 molecules in total (60 surface Si atoms) with amorphous structure (atomic density 2.33 g/cm^3). Si atoms on the surface of each NM are initially terminated with dangling bonds without bonding to hydrogen or hydroxide and with occasional $Si-O^-$ termination for the SiO_2 NM (16%). Figure 5b describes the water permeation event, as defined by transmission of a water molecule through the NM from one side of the water bath to the other side (see Figure 5a). No permeation is observed in Si NM over the simulation time of ~12 ns in 10 simulation replicas owing to the hermetic, crystalline structure of the material. Si surface atoms, initially with dangling bonds, form chemical bonds with OH^- from water molecules, as shown in Figure 5b. Formation of Si−O−Si bonds occurs due to the nucleophilic attack of O from OH-terminated Si to nearby surface Si atoms with dangling bonds. Roughly 30%

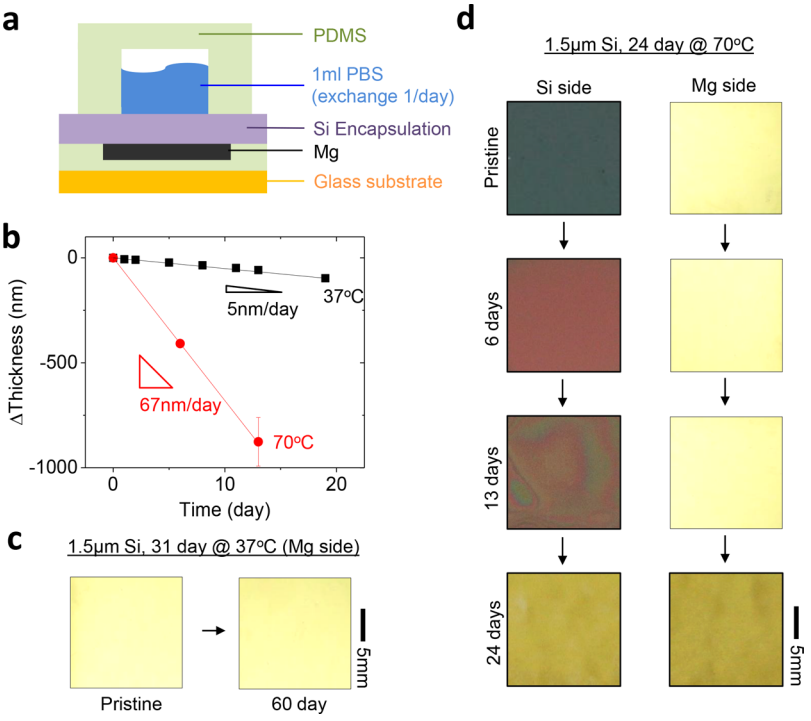

Figure 3. Si NMs as water-soluble water barriers. (a) Experimental setup in which a thin Mg pad allows direct imaging of the penetration of water through an overlying Si NM barrier layer. (b) Change in thickness with the operational condition. (c) Optical images of the Mg at various times at 37 °C. (d) Optical images of Si and Mg pad at 70 °C.

DOI: 10.1021/acsnano.7b06697
ACS Nano 2017, 11, 12562−12572

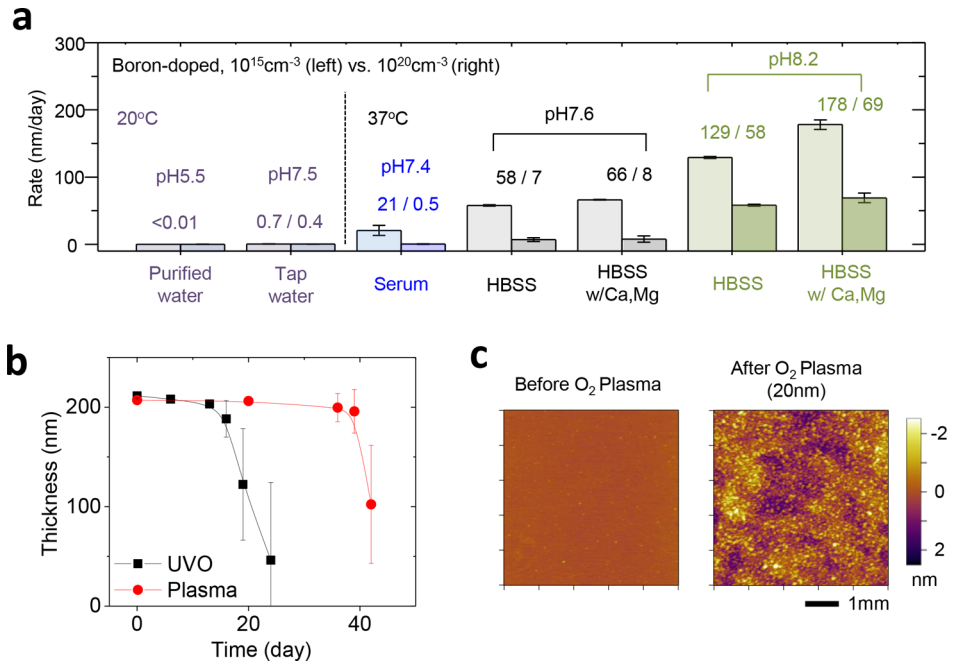

Figure 4. Strategies for controlling the lifetime of a Si NM barrier layer. (a) Rates of dissolution of p^+-Si (boron, 10^{20} cm^{-3}). (b) Change in thickness of a p-Si NM in PBS. (c) Atomic force microscopy images of the surface of the p-Si.

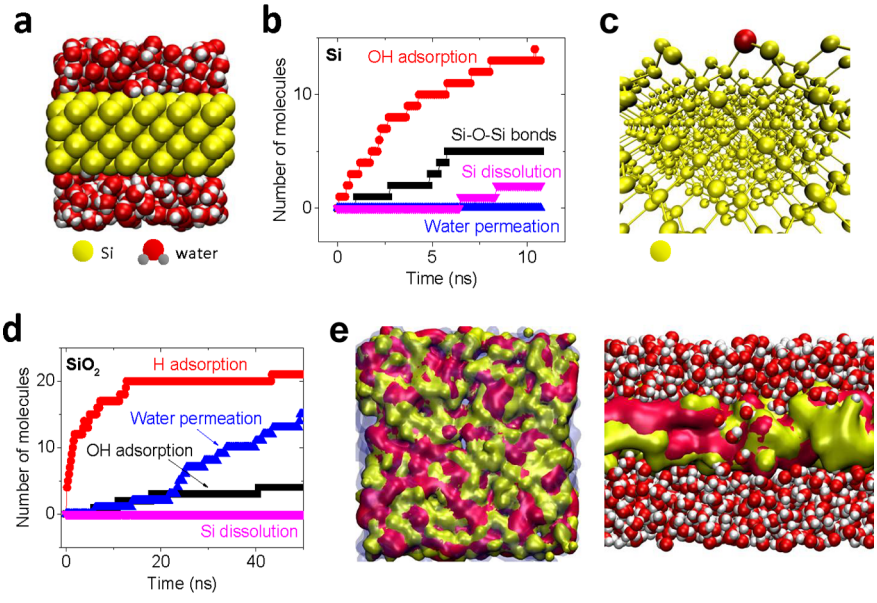

Figure 5. Reactive molecular dynamics simulation of Si (1 nm) and SiO_2 (1.25 nm) NMs in water. (a) Initial structure of the Si NM. (b) Reaction products for the Si NM. (c) Si−O−Si formation on the Si surface. (d) Reaction products for the SiO_2 NM. (e) Water permeation through the SiO_2 NM. Top view (left) and cross-sectional view (right).

of OH^- adsorbed on the Si surface creates Si−O−Si bonds, as shown in Figure 5c. The formation of $Si(OH)_2$ on the surface of the Si is also possible, which accounts for 42% of the OH^- adsorption. Dissociation of three Si atoms from the Si NM occurs from these $Si(OH)_2$ as a form of $Si(OH)_2^{2+}$, which eventually converts to $Si(OH)_4$ by interactions with surrounding water. Notably, no dissolution is observed from the Si atoms in Si−O−Si bonds, as expected based on the higher stability of SiO_2 against hydrolysis compared to Si. Concurrent oxidation and dissolution is consistent with a previous experimental report result on lightly doped Si.[32] Figure 5d compares the same type of dynamic changes in SiO_2 NMs. Due to the amorphous structure of the slab, water begins to permeate through the SiO_2 NMs after a couple of nanoseconds. Water channels (Figure 5e) spontaneously form at 6 and 23 ns, as indicated by a sharp increase in water permeation in Figure 5d. The presence of initial voids in the SiO_2 structure, as distinct from the crystalline order in the Si NMs, leads to the channel formation. The average time for a single water molecule to permeate through the SiO_2 is 7.23 ns. Adsorption of H on the SiO_2 occurs due to rapid bond formation between H^+ and oxygen-terminated Si atoms.

In addition to use as a bioresorbable barrier layer, Si NMs can simultaneously serve as the foundation for thin, flexible

DOI: 10.1021/acsnano.7b06697
ACS Nano 2017, 11, 12562−12572

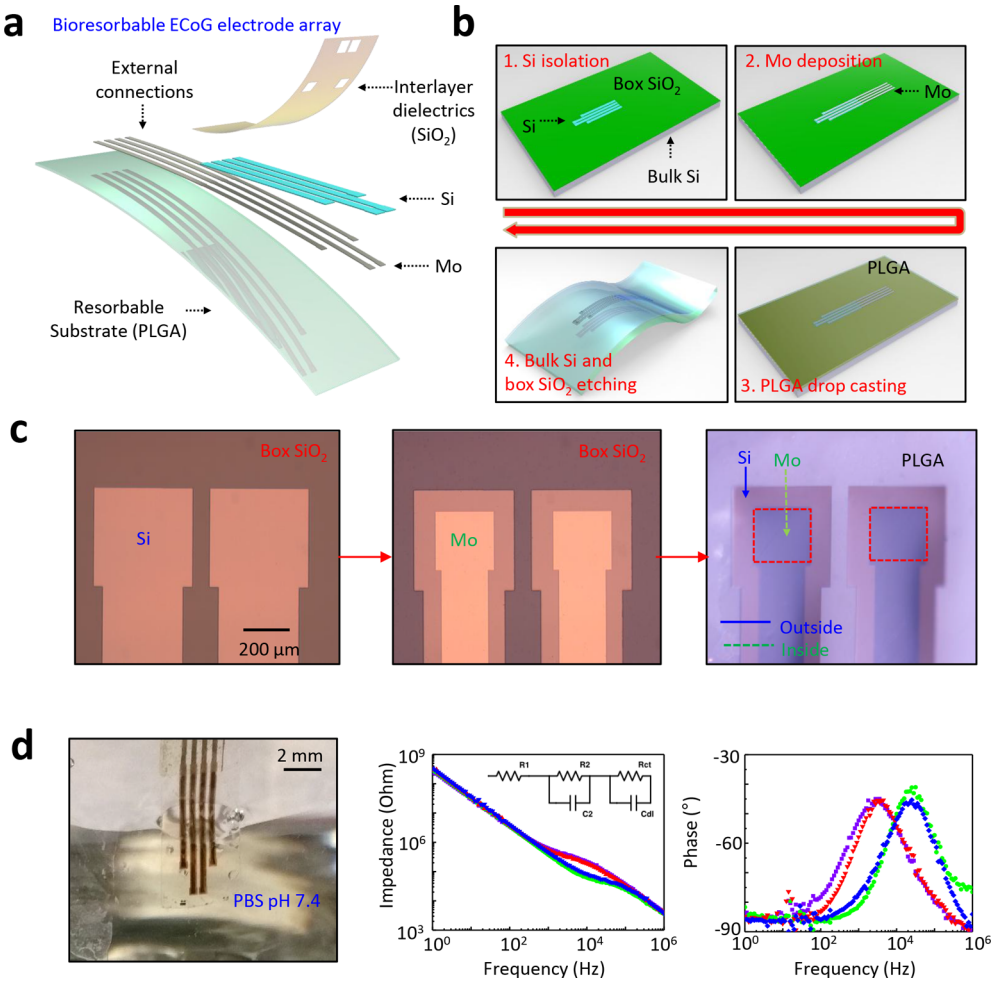

Figure 6. Thin, flexible neural electrode arrays with fully bioresorbable construction by use of doped Si NMs. (a) Schematic exploded-view illustration of a passive array for electrocorticography. (b) Fabrication process. (c) Optical images of the device. (d) Electrochemical impedance spectrum of four electrodes in PBS solution.

biosensing electrodes, as illustrated in Figure 6, with a demonstration that uses coatings of Mo underneath patterned Si NMs (10^{15} cm^{-3}, 1.5 μm). Mo metal without the Si NM on top undergoes comparatively fast dissolution, with a tendency to crack, fragment, and flake in biofluids (Figure S5). Figure 6a presents an exploded schematic diagram of the device structure. Here, a layer of SiO_2 defines openings to the Si for four measurement sites for electrocorticography (ECoG) on rat cortex. A flexible sheet of the bioresorbable polymer (PLGA) serves as the substrate. The fabrication processes appear in Figure 6b. The first step involves isolation of the Si layer on an SOI wafer, followed by deposition of Mo electrodes. After drop-casting PLGA on the electrodes, back-etching of the bulk Si and buried SiO_2 yields a flexible and bioresorbable neural sensing array. A final layer of 50 nm of SiO_2 defines the sensing areas (250 × 250 μm). Optical micrographs in Figure 6c highlight the structure of the electrodes. The area of Si NM encapsulation is slightly larger than that of the Mo electrodes to ensure protection against water penetration from the side edges. Electrochemical impedance spectra (EIS) collected at room temperature in PBS solutions simulate the interface characteristics between neural electrodes and brain tissues. The magnitude of the impendance and its phase angle for the four electrodes are in Figure 6d. At frequencies most relevant for neural sensing (near 1 kHz), the magnitude varies between 380 and 620 kΩ. The phase angle suggests capacitive (~90°) behavior at low frequencies (1−10 Hz), with less capacitive behavior (~45°) at fequencies near 1 kHz. An equivalent Randles circuit with the addition of a resistor in parallel with a capcitor captures the impedance spectra of Si/Mo electrodes (Figure S4b). The additional capacitor might suggest a Schottky barrier at the Mo/Si interface.[41] The interface charge transfer resistance, R_{ct}, and double layer capacitance, C_{dl}, are found, from fitting, to be 2.2 GΩ and 0.45 nF, respectively. The lifetime of the current Si electrodes (10^{15} cm^{-3}, 1.5 μm) is expected to be ~50 days at 37 °C based on the abrupt change in the electrode EIS in accelerated tests at 70 °C at 4 days (Figure S5).

In vivo neural recordings with these types of bioresorbable neural sensors in adult rat animal models demonstrate good performance. The electrode array (4 sites) and a control electrode rest on the right barrel cortex of an anesthetized rat, as illustrated in Figure 7a. Representative 5 s segments of ECoG recordings of sleep spindle activity are shown in Figure 7b. The up−down dynamics at ~1 Hz with high-frequency oscillations occurring during the up states is typical of the sleep-like state induced by ketamine−dexmedetomidine anesthesia. Consistently, the power spectra of these recordings (Figure 7c) show two clear physiological peaks, one at 0.5−2 Hz (up−down state) and the other at 30−90 Hz (gamma-frequency oscillations in the up states), without discernible difference or signal attenuation in any frequency band between the bioresorbable and control electrodes.

DOI: 10.1021/acsnano.7b06697
ACS Nano 2017, 11, 12562−12572

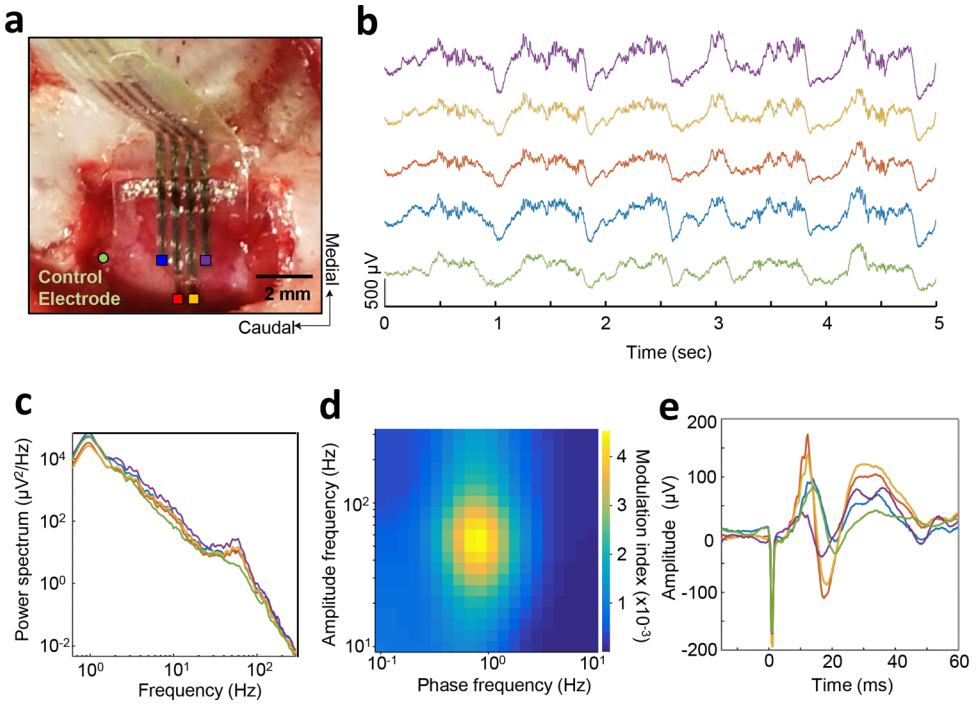

Figure 7. ***In vivo*** **neural recordings in rats using a passive, bioresorbable electrode array. (a) Photograph of the electrode array on the right barrel cortex of an anesthetized rat. The colored boxes highlight the electrode contacts. A control electrode (green circle; electrode not present in photo) resides next to the next to the bioresorbable array. (b) Representative segment of cortical recordings from the four electrodes and the control electrode. (c) Power spectra of the recordings. (d) Comodulogram quantifying strong phase amplitude coupling between different neural oscillations. (e) Recorded cortical evoked response to electrical stimulation of a focal portion of the contralateral whisker pad. Sharp negative potential near 0 ms is the stimulus artifact.**

The comodulogram in Figure 7d shows strong coupling between the phase of the up−down state and the amplitude of the gamma oscillations.[41] The bioresorbable electrode can also be used for cortical recordings of somatosensory-evoked potentials (EPs). Figure 7e shows the cortical response to a focal electrical stimulation of the contralateral whisker pad recorded with the bioresorbable and the control electrodes. The response consists in a stimulus artifact near 0 ms followed by biphasic EPs at ∼7 ms latency, consistent with previous reports.[42] Collectively, all recordings with the bioresorbable electrodes are comparable to those of the control electrode.

CONCLUSION

The results presented here reveal the dependence of the rate of dissolution of Si NMs on protein, $Si(OH)_4$ and Ca^{2+} in surrounding aqueous solutions. The results indicate a decelerating effect of $Si(OH)_4$ and proteins, and ion-specific accelerating effects of Ca^{2+}. Uniform, controlled dissolution over large areas enables the use of Si NMs as bioresorbable water barriers, of utility in temporary electronic implants and environmental monitors. Strategies for extending the lifetimes of such types of barriers include the addition of dopants into the silicon or the growth of oxides onto its surface. The mechanical flexibility of doped Si NMs allows additional use as a bioresorbable electrode interfaces for biopotential measurements, as demonstrated through *in vivo* measurements of ECoG signals in rodent models. These collective findings have relevance to the further development of bio- and eco-resorbable forms of electronics.

EXPERIMENTAL METHODS

Dissolution of Si Nanomembranes. The time-dependent changes in the thickness of Si nanomembranes (200 nm initial thickness) on SOI wafers (p-type (boron), 8.5−11.5 Ω·cm, (100), SOITEC) defined the dissolution rates. UVO cleaning (10 min) followed by removal of the surface oxide by immersion in buffered oxide etchant (2 min) prepared the silicon surface for the dissolution tests.[15] Soaking tests used various types of simulated biofluids including PBS (Corning cellgro), Hank's balanced salt solution (Thermo Fisher Scientific), bovine serum (RMBIO), and artificial perspiration (Pickering Laboratories) at room temperature (∼20 °C) or at 37 °C. All solutions were stored in PETE bottles as purchased, and experiments were conducted in high-density polyethylene bottles (United States Plastic Corp.). The thickness of the Si NM was determined either by reflectometry (MProbe, Semicon Soft) or profilometry (Veeco/Sloan Dektak 3 ST, Plainview) after the soaking tests. Dissolution tests with highly doped silicon and with silicon coated with surface oxide followed the same procedures except for the silicon preparation steps. Highly doped silicon (p-type, boron, 10^{20} cm^3) was prepared by solid state diffusion (1050 °C, 15 min). Surface oxides were grown through exposure to O_2 plasma (200 mT, 250 W, 20 min) or UV-induced ozone (10 min). Thickness of oxide was measured by spectroscopic ellipsometry (J.A. Woollam Co. Inc., USA). Atomic force microscopy (Asylum Research MFP-3D) defined the surface morphology of the SiO_2 grown by O_2 plasma before and after dissolution.

Si NM Encapsulation in Biofluids. Photolithographic patterning of electron beam evaporated layers of Ti/Mg (50/200 nm) defined traces on SOI wafers with top Si layers with thicknesses of 1.5 μm. Casting a layer of polyimide (PI-2545, HD MicroSystems; 3.5 μm) on the front side of such a substrate, laminating it against a glass substrate coated with poly(dimethylsiloxane) (PDMS; 10 μm), and then inductively coupled plasma reactive ion etching (ICP-RIE, Surface Technology System) with gas flow of SF_6/O_2 with 40/3 sccm at a pressure of 50 mTorr removed the silicon wafer. Eliminating the buried oxide layer with HF left only the 1.5 μm silicon membrane. A PDMS chamber bonded to the Si served to confine the PBS solutions. The solutions were replaced every day to avoid changes in dissolution rate associated with buildup of reaction products.

Reactive Molecular Dynamics Simulation. To model atomic scale interaction between Si/SiO_2 and water, RMD simulations were

DOI: 10.1021/acsnano.7b06697
ACS Nano 2017, 11, 12562−12572

performed with the Reaxff potential,[43] integrated in the large-scale atomic/molecular massively parallel simulator (LAMMPS) package.[44] Previous studies show that the reactive potential developed for the Si/SiO_2 interaction with water can reproduce the macroscale experimental properties of these interfaces.[45] The elements in our simulations are silicon, oxygen, and hydrogen. Two initial systems for Si and SiO_2 NMs were created: Si NM with 602 silicon atoms (1.2 nm thickness) solvated with 3130 water molecules; SiO_2 NM with 283 SiO_2 molecules (1.25 nm thickness) solvated with 3119 water molecules. Periodic boundary conditions were used in all directions. Energy minimization of the system was performed for 1000000 steps. To ensure the capture of chemical reaction events between different atomic species, the time step was 0.1 fs.[46] The Nosé-Hoover thermostat maintained the temperature at T = 300 K. The simulation was run for 50 ns, and data were collected with the frequency of 0.1 ps. To compute the adsorption of H^+ or OH^- groups in the simulations, we computed the root-mean-square displacement (rmsd) of H^+ or OH^- between the simulation frames. At the adsorption event, the rmsd drops sharply from the average of 13.5 to 0.92 Å. Only H^+ or OH^- with distance less than 2.8 Å from surface silicon atoms were considered adsorbed. To count the number of dissociated Si from the crystal structures, the rmsd of each Si is monitored in each simulation step. The rmsd of the silicon atom in the crystal structure is 1.1 Å. When a Si atom is dissociated, its rmsd sharply increases to >10 Å.

Fabrication of ECoG Arrays. The process began with thinning the handle substrate of an SOI wafer (1.5 μm top Si layer) by mechanical grinding to a thickness of 150 μm. The top Si on the SOI wafer was then patterned by photolithography (AZ 5214) and reactive ion etching (RIE) with SF_6 gas, to define the encapsulation layer. A thin film of Mo (300 nm) was deposited on the membrane by magnetron sputtering (AJA Orion 8 evaporation system, N. Scituate, MA) and patterned by photolithography (AZ nLOF 2070). Next, PLGA (~30 μm, lactide/glycolide ratio of 75:25) was drop-cast on the top surface, and then the wafer and buried oxide were removed by etching with XeF_2 (XACTIX system) and buffered oxide (BOE, 6:1), respectively. Finally, a layer of SiO_2 was deposited by electron beam evaporation and patterned to define the sensing area for the neural electrodes (250 × 250 μm). An ACF cable bonded to the terminal regions of the neural electrodes served as connection interfaces to external data acquisition (DAQ) systems.

EIS Measurements. Electrochemical impedance spectra of the ECoG neural electrodes were measured in PBS solutions to define the interface impedance characteristics (1−1 MHz, 10 mV amplitude, 0 V bias from open circuit voltage, Gamry Reference 600 potentiostat, EIS 300 frequency analyzer). Long-term accelerated soaking tests were also performed at 70 °C in PBS solutions to examine the effectiveness of Si NM encapsulation. Neural electrodes with Si NM encapsulation were fabricated through similar fabrication steps, except that glass substrates with PDMS adhesive instead of PLGA films were bonded to SOI surface, to avoid possible deformation induced by PLGA polymer at elevated temperature. For Mo-only neural electrodes, Mo was deposited directly on glass substrates. Parylene (1 μm) instead of SiO_2 was deposited as a final layer to define the electrode sensing area, to minimize water permeation to the other areas of the electrodes. ACF cable was bonded to the terminal regions of the neural electrodes to connect to the potentiostat. Optical micrographs and EIS were collected at different soaking times, to compare the lifetime of neural electrodes with and without Si encapsulation.

***In Vivo* Neural Recording.** The following procedures were approved by the Institutional Animal Care and Use Committee of the University of Pennsylvania. One 225 g Sprague−Dawley rat was anesthetized with a ketamine (60 mg kg^{-1}) and dexdomitor (0.25 mg kg^{-1}) solution and placed in a stereotaxic frame. A craniotomy was performed to expose the right barrel cortex. A skull screw was placed in the left parietal bone to serve as the reference electrode for the recordings. The recording array was placed over the exposed cortical surface. A control electrode (200 μm diameter, tungsten) was placed on the cortical surface caudal to the array. Simultaneous neural recordings from the five electrodes were performed with a commercial electrophysiology system (Tucker-Davis Technologies) at a sampling frequency of 25 kHz. To elicit cortical evoked responses, a pair of needle stimulating electrodes were inserted into the left mystacial pad. Brief electrical pulses (500 μA, 1 ms, monophasic) were used to activate the intrinsic muscles of the vibrissae, causing a visible protraction of a whisker.

ASSOCIATED CONTENT

Supporting Information

The Supporting Information is available free of charge on the ACS Publications website at DOI: 10.1021/acsnano.7b06697.

Figures that summarize the chemical composition of the simulated biofluids; data on the spectral reflectance and surface profile of the SOI wafer; the encapsulation of the Mg pad with PLGA and electron-beam deposited SiO_2; the SiO_2 growth by exposure to UV ozone and O_2 plasma; EIS and surface morphologies of Mo and Mo/Si electrodes (PDF)

AUTHOR INFORMATION

Corresponding Authors

*E-mail: lanyin@tsinghua.edu.cn.
*E-mail: jrogers@northwestern.edu.

ORCID

Amir Barati Farimani: 0000-0002-2952-8576
Yongfeng Mei: 0000-0002-3314-6108
Xue Feng: 0000-0001-9242-8474
Lan Yin: 0000-0001-7306-4628

Author Contributions

[‡]Y.K.L. and K.J.Y. contributed equally to this work.

Notes

The authors declare no competing financial interest.

ACKNOWLEDGMENTS

Y.K.L. would like to thank the support from Kwanjeong Educational Foundation. K.J.Yu acknowledges the support from the National Research Foundation of Korea (NRF2017M1A2A2048904). Z.X. and X.F. acknowledge the support from the National Basic Research Program of China (Grant No. 2015CB351900) and National Natural Science Foundation of China (Grant Nos. 11402134 and 11320101001). Y.H. acknowledges the support from NSF (Grant Nos. 1400169, 1534120, and 1635443) and NIH (Grant No. R01EB019337). B.L. acknowledges NIH U01-NS094340, Mirowski Family Foundation, and Neil and Barbara Smit, and F.V. acknowledges Citizens United for Research in Epilepsy Taking Flight Award. L. Y. acknowledges the support from National Natural Science Foundation of China (NSFC, Grant No. 51601103) and 1000 Youth Talents Program in China.

REFERENCES

(1) Hwang, S.-W.; Tao, H.; Kim, D.-H.; Cheng, H.; Song, J.-K.; Rill, E.; Brenckle, M. A.; Panilaitis, B.; Won, S. M.; Kim, Y.-S.; Song, Y. M.; Yu, K. J.; Ameen, A.; Li, R.; Su, Y.; Yang, M.; Kaplan, D. L.; Zakin, M. R.; Slepian, M. J.; Huang, Y.; Omenetto, F. G.; Rogers, J. A. A Physically Transient Form of Silicon Electronics. *Science* **2012**, *337*, 1640−1644.

(2) Hwang, S.-W.; Huang, X.; Seo, J.-H.; Song, J.-K.; Kim, S.; Hage-Ali, S.; Chung, H.-J.; Tao, H.; Omenetto, F. G.; Ma, Z.; Rogers, J. A. Materials for Bioresorbable Radio Frequency Electronics. *Adv. Mater.* **2013**, *25*, 3526−3531.

(3) Hwang, S.-W.; Park, G.; Cheng, H.; Song, J.-K.; Kang, S.-K.; Yin, L.; Kim, J.-H.; Omenetto, F. G.; Huang, Y.; Lee, K.-M.; Rogers, J. A. 25th Anniversary Article: Materials for High-Performance Biodegradable Semiconductor Devices. *Adv. Mater.* **2014**, *26*, 1992−2000.

DOI: 10.1021/acsnano.7b06697
ACS Nano 2017, 11, 12562−12572

(4) Yin, L.; Huang, X.; Xu, H.; Zhang, Y.; Lam, J.; Cheng, J.; Rogers, J. A. Materials, Designs, and Operational Characteristics for Fully Biodegradable Primary Batteries. *Adv. Mater.* **2014**, *26*, 3879−3884.
(5) Yu, K. J.; Kuzum, D.; Hwang, S.-W.; Kim, B. H.; Juul, H.; Kim, N. H.; Won, S. M.; Chiang, K.; Trumpis, M.; Richardson, A. G.; Cheng, H.; Fang, H.; Thompson, M.; Bink, H.; Talos, D.; Seo, K. J.; Lee, H. N.; Kang, S.-K.; Kim, J.-H.; Lee, J.-Y.; Huang, Y.; Jensen, F. E.; Dichter, M.; Lucas, T. H.; Viventi, J.; Litt, B.; Rogers, J. A. Bioresorbable Silicon Electronics for Transient Spatiotemporal Mapping of Electrical Activity from the Cerebral Cortex. *Nat. Mater.* **2016**, *15*, 782−791.
(6) Yin, L.; Farimani, A. B.; Min, K.; Vishal, N.; Lam, J.; Lee, Y. K.; Aluru, N. R.; Rogers, J. A. Mechanisms for Hydrolysis of Silicon Nanomembranes as Used in Bioresorbable Electronics. *Adv. Mater.* **2015**, *27*, 1857−1864.
(7) Yin, L.; Cheng, H.; Mao, S.; Haasch, R.; Liu, Y.; Xie, X.; Hwang, S. W.; Jain, H.; Kang, S. K.; Su, Y.; Li, R.; Huang, Y.; Rogers, J. A. Dissolvable Metals for Transient Electronics. *Adv. Funct. Mater.* **2014**, *24*, 645−658.
(8) Kang, S. K.; Hwang, S. W.; Cheng, H.; Yu, S.; Kim, B. H.; Kim, J. H.; Huang, Y.; Rogers, J. A. Dissolution Behaviors and Applications of Silicon Oxides and Nitrides in Transient Electronics. *Adv. Funct. Mater.* **2014**, *24*, 4427−4434.
(9) Hwang, S.-W.; Park, G.; Edwards, C.; Corbin, E. A.; Kang, S.-K.; Cheng, H.; Song, J.-K.; Kim, J.-H.; Yu, S.; Ng, J.; Lee, J. E.; Kim, J.; Yee, C.; Bhaduri, B.; Su, Y.; Omennetto, F.; Huang, Y.; Bashir, R.; Goddard, L.; Popescu, G.; Lee, K.-M; Rogers, J. A. Dissolution Chemistry and Biocompatibility of Single-Crystalline Silicon Nanomembranes and Associated Materials for Transient Electronics. *ACS Nano* **2014**, *8*, 5843−5851.
(10) Angermann, H.; Henrion, W.; Rebien, M.; Röseler, A. Wet-Chemical Preparation and Spectroscopic Characterization of Si Interfaces. *Appl. Surf. Sci.* **2004**, *235*, 322−339.
(11) Sawada, Y.; Tsujino, K.; Matsumura, M. Hydrogen Evolution from Atomically Flat Si(111) Surfaces Exposed to 40% NH_4F, Oxygen-Free Water, or Wet Gas. *J. Electrochem. Soc.* **2006**, *153*, C854−C857.
(12) Sugimoto, F.; Okamura, S. Adsorption Behavior of Organic Contaminants on a Silicon Wafer Surface. *J. Electrochem. Soc.* **1999**, *146*, 2725−2729.
(13) Sachon, E.; Matheron, L.; Clodic, G.; Blasco, T.; Bolbach, G. MALDI TOF-TOF Characterization of a Light Stabilizer Polymer Contaminant from Polypropylene or Polyethylene Plastic Test Tubes. *J. Mass Spectrom.* **2010**, *45*, 43−50.
(14) Zhang, X. G. *Electrochemistry of Silicon and Its Oxide*; Kluwer Academic Publishers: New York, 2001; pp 279−351.
(15) Takahagi, T.; Nagai, I.; Ishitani, A.; Kuroda, H.; Nagasawa, Y. The Formation of Hydrogen Passivated Silicon Single-Crystal Surfaces Using Ultraviolet Cleaning and HF Etching. *J. Appl. Phys.* **1988**, *64*, 3516−3521.
(16) Kang, S.-K.; Murphy, K. J.; Hwang, S.-W.; Lee, S. M.; Harburg, D. V.; Krueger, N. A.; Shin, J.; Gamble, P.; Cheng, H.; Yu, S.; Liu, Z.; McCall, J.; Stephen, M.; Ying, H.; Kim, J.; Park, G.; Webb, C.; Lee, C. H.; Chung, S.; Wie, D. S.; Gujar, A. D.; Vemulapalli, B.; Kim, A. H.; Lee, K.-M.; Cheng, J.; Huang, Y.; Lee, S. H.; Braun, P. V.; Ray, W. Z.; Rogers, J. A. Bioresorbable Silicon Electronic Sensors for the Brain. *Nature* **2016**, *530*, 71−76.
(17) Lee, G.; Kang, S.-K.; Won, S. M.; Gutruf, P.; Jeong, Y. R.; Koo, J.; Lee, S.-S.; Rogers, J. A.; Ha, J. S. Fully Biodegradable Micro-supercapacitor for Power Storage in Transient Electronics. *Adv. Energy Mater.* **2017**, *7*, 1700157.
(18) Krause, U.; Raunio, V. Protein Content of Normal Human Aqueous Humour *in Vivo*. *Acta Ophthalmol.* **1969**, *47*, 215−221.
(19) Fogh-Andersen, N.; Altura, B. M.; Altufu, B. T.; Siggaard-Andersen, O. Composition of Interstitial Fluid. *Clin. Chem.* **1995**, *41*, 1522−1525.
(20) Nakanishi, K.; Sakiyama, T.; Imamura, K. Review on the Adsorption of Proteins on Solid Surfaces, a Common but Very Complicated Phenomenon. *J. Biosci. Bioeng.* **2001**, *91*, 233−244.
(21) Sofia, S. J.; Premnath, V.; Merrill, E. W. Poly(ethylene Oxide) Grafted to Silicon Surfaces: Grafting Density and Protein Adsorption. *Macromolecules* **1998**, *31*, 5059−5070.
(22) Sharma, S.; Johnson, R. W.; Desai, T. A. Evaluation of the Stability of Nonfouling Ultrathin Poly(ethylene Glycol) Films for Silicon-Based Microdevices. *Langmuir* **2004**, *20*, 348−356.
(23) Icopini, G. A.; Brantley, S. L.; Heaney, P. J. Kinetics of Silica Oligomerization and Nanocolloid Formation as a Function of pH and Ionic Strength at 25°C. *Geochim. Cosmochim. Acta* **2005**, *69*, 293−303.
(24) Fleming, B. A. Kinetics of Reaction between Silicic Acid and Amorphous Silica Surfaces in NaCl Solutions. *J. Colloid Interface Sci.* **1986**, *110*, 40−64.
(25) Dove, P. M.; Han, N.; De Yoreo, J. J. Mechanisms of Classical Crystal Growth Theory Explain Quartz and Silicate Dissolution Behavior. *Proc. Natl. Acad. Sci. U. S. A.* **2005**, *102*, 15357−15362.
(26) Dove, P. M.; Han, N.; Wallace, A. F.; De Yoreo, J. J. Kinetics of Amorphous Silica Dissolution and the Paradox of the Silica Polymorphs. *Proc. Natl. Acad. Sci. U. S. A.* **2008**, *105*, 9903−9908.
(27) Gunnarsson, I.; Arnorsson, S. Amorphous Silica Solubility and the Thermodynamic Properties of H_4SiO_4 in the Range of 0° to 350°C at P_{Sat}. *Geochim. Cosmochim. Acta* **2000**, *64*, 2295−2307.
(28) Sugimoto, F.; Okamura, S. Adsorption Behavior of Organic Contaminants on a Silicon Wafer Surface. *J. Electrochem. Soc.* **1999**, *146*, 2725−2729.
(29) Fukidome, H.; Matsumura, M.; Komeda, T.; Namba, K.; Nishioka, Y. *In situ* Atomic Force Microscopy Observation of Dissolution Process of Si(111) in Oxygen-free Water at Room Temperature. *Electrochem. Solid-State Lett.* **1999**, *2*, 393−394.
(30) Palik, E. D.; Faust, J. W.; Gray, H. F.; Greene, R. F. Study of the Etch-Stop Mechanism in Silicon. *J. Electrochem. Soc.* **1982**, *129*, 2051−2059.
(31) Palik, E. D.; Bermudez, V. M.; Glembocki, O. J. Ellipsometric Study of the Etch-Stop Mechanism in Heavily Doped Silicon. *J. Electrochem. Soc.* **1985**, *132*, 135−141.
(32) Morita, M.; Ohmi, T.; Hasegawa, E.; Kawakami, M.; Ohwada, M. Growth of Native Oxide on a Silicon Surface. *J. Appl. Phys.* **1990**, *68*, 1272−1281.
(33) Ciacchi, L. C.; Payne, M. C. First-Principles Molecular-Dynamics Study of Native Oxide Growth on Si(001). *Phys. Rev. Lett.* **2005**, *95*, 196101.
(34) Wallace, A. F.; Gibbs, G. V.; Dove, P. M. Influence of Ion-Associated Water on the Hydrolysis of Si-O Bonded Interactions. *J. Phys. Chem. A* **2010**, *114*, 2534−2542.
(35) Ebeling, D.; van den Ende, D.; Mugele, F. Electrostatic Interaction Forces in Aqueous Salt Solutions of Variable Concentration and Valency. *Nanotechnology* **2011**, *22*, 305706.
(36) Rimstidt, J. D. Rate Equations for Sodium Catalyzed Quartz Dissolution. *Geochim. Cosmochim. Acta* **2015**, *167*, 195−204.
(37) Brady, P. V.; Walther, J. V. Kinetics of Quartz Dissolution at Low Temperatures. *Chem. Geol.* **1990**, *82*, 253−264.
(38) Fang, H.; Zhao, J.; Yu, K. J.; Song, E.; Farimani, A. B.; Chiang, C.-H.; Jin, X.; Xue, Y.; Xu, D.; Du, W.; Seo, K. J.; Zhong, Y.; Yang, Z.; Won, S. M.; Fang, G.; Choi, S. W.; Chaudhuri, S.; Huang, Y.; Alam, M. A.; Viventi, J.; Aluru, N. R.; Rogers, J. A. Ultrathin, Transferred Layers of Thermally Grown Silicon Dioxide as Biofluid Barriers for Biointegrated Flexible Electronic Systems. *Proc. Natl. Acad. Sci. U. S. A.* **2016**, *113*, 11682−11687.
(39) Wayner, D. D. M.; Wolkow, R. A. Organic Modification of Hydrogen Terminated Silicon Surfaces. *J. Chem. Soc. Perkin Trans. 2* **2002**, *0*, 23−34.
(40) Anglin, E. J.; Cheng, L.; Freeman, W. R.; Sailor, M. J. Porous Silicon in Drug Delivery Devices and Materials. *Adv. Drug Delivery Rev.* **2008**, *60*, 1266−1277.
(41) Kano, G.; Inoue, M.; Matsuno, J.; Takayanagi, S. Molybdenum-Silicon Schottky Barrier. *J. Appl. Phys.* **1966**, *37*, 2985−2987.
(42) Di, S.; Baumgartner, C.; Barth, D. S. Laminar Analysis of Extracellular Field Potentials in Rat Vibrissa/Barrel Cortex. *J. Neurophysiol.* **1990**, *63*, 832−840.

DOI: 10.1021/acsnano.7b06697
ACS Nano 2017, 11, 12562−12572

(43) van Duin, A. C. T.; Dasgupta, S.; Lorant, F.; Goddard, W. A. ReaxFF: A Reactive Force Field for Hydrocarbons. *J. Phys. Chem. A* **2001**, *105*, 9396−9409.
(44) Plimpton, S. Fast Parallel Algorithms for Short-Range Molecular Dynamics. *J. Comput. Phys.* **1995**, *117*, 1−19.
(45) Fogarty, J. C.; Aktulga, H. M.; Grama, A. Y.; van Duin, A. C. T.; Pandit, S. A. A Reactive Molecular Dynamics Simulation of the Silica-Water Interface. *J. Chem. Phys.* **2010**, *132*, 174704.
(46) van Duin, Adri C. T.; Strachan, Alejandro; Stewman, Shannon; Zhang, Qingsong; Xu, Xin; Goddard, William A. ReaxFFSiO Reactive Force Field for Silicon and Silicon Oxide Systems. *J. Phys. Chem. A* **2003**, *107*, 3803−3811.

DOI: 10.1021/acsnano.7b06697
ACS Nano 2017, 11, 12562−12572